

UC San Diego

UC San Diego Previously Published Works

Title

Volumetric segmentation-free method for rapid visualization of vascular wall shear stress using 4D flow MRI

Permalink

<https://escholarship.org/uc/item/52s7586k>

Journal

Magnetic Resonance in Medicine, 80(2)

ISSN

0740-3194

Authors

Masutani, Evan M
Contijoch, Francisco
Kyubwa, Espoir
[et al.](#)

Publication Date


2018-08-01

DOI

10.1002/mrm.27159

Peer reviewed

Volumetric segmentation-free method for rapid visualization of vascular wall shear stress using 4D flow MRI

Evan M. Masutani^{1,2} | Francisco Contijoch^{3,4}  | Espoir Kyubwa^{1,2} | Joseph Cheng⁵  | Marcus T. Alley⁵ | Shreyas Vasanawala⁵ | Albert Hsiao⁴ 

¹Medical Scientist Training Program, University of California, San Diego, La Jolla, California, USA

²Department of Medicine, University of California, San Diego, La Jolla, California, USA

³Department of Bioengineering, University of California, San Diego, La Jolla, California, USA

⁴Department of Radiology, University of California, San Diego, La Jolla, California, USA

⁵Department of Radiology, Stanford University, Stanford, California, USA

Correspondence

Albert Hsiao, UC San Diego, 9300 Campus Point Drive, MC 0841, San Diego, CA 92037-0841
Email: a3hsiao@mail.ucsd.edu

Funding information

E.M.M. is supported by the UC San Diego Medical Scientist Training Program (NIH Grant T32GM007198). A. H. is supported by a research grant from GE Healthcare

Purpose: To develop a rapid segmentation-free method to visualize and compute wall shear stress (WSS) throughout the aorta using 4D Flow MRI data. WSS is the drag force-per-area the vessel endothelium exerts on luminal blood; abnormal levels of WSS are associated with cardiovascular pathologies. Previous methods for computing WSS are bottlenecked by labor-intensive manual segmentation of vessel boundaries. A rapid automated segmentation-free method for computing WSS is presented.

Theory and Methods: Shear stress is the dot-product of the viscous stress tensor and the inward normal vector. The inward normal vectors are approximated as the gradient of fluid speed at every voxel. Subsequently, a 4D map of shear stress is computed as the partial derivatives of velocity with respect to the inward normal vectors. We highlight the shear stress near the wall by fusing visualization with edge-emphasized anatomical data.

Results: As a proof-of-concept, four cases with aortic pathologies are presented. Visualization allows for rapid localization of pathologic WSS. Subsequent analysis of these pathological regions enables quantification of WSS. Average WSS during peak systole measures approximately 50–60 cPa in nonpathological regions of the aorta and is elevated in regions of stenosis, coarctation, and dissection. WSS is reduced in regions of aneurysm.

Conclusion: A volumetric technique for calculation and visualization of WSS from 4D Flow MRI data is presented. Traditional labor-intensive methods for WSS rely on explicit manual segmentation of vessel boundaries before visualization. This automated volumetric strategy for visualization and quantification of WSS may facilitate its clinical translation.

KEYWORDS

wall shear stress, cardiovascular, computational, 4D Flow MRI, segmentation-free

1 | INTRODUCTION

Wall shear stress (WSS) is implicated in a variety of cardiovascular diseases, including atherosclerosis, aortic dissection, and aneurysm formation.^{1–4} While inflammation and the buildup of low-density lipoprotein cholesterol are the more commonly associated features of cardiovascular disease, pathological WSS may lie upstream of these processes.¹ WSS is the drag force per area the endothelium exerts on luminal fluid and is impacted by vascular geometry, turbulent flow, and other hemodynamic disruptions. Cellular mechanotransducers may sense altered shear stress and actuate changes in vascular cell state.¹ Altered WSS is associated with changes in production of vasodilatory vascular endothelial nitric oxide synthase, inflammatory processes, and endothelial structural integrity.¹ It may, therefore, be beneficial to routinely evaluate wall shear stress in patients with cardiovascular disease.

WSS is physically defined as the change in fluid velocity at the endothelium in the direction of the vessel lumen. Computation of WSS, therefore, requires spatially resolved velocity data as well as demarcation of the endothelial boundaries. 4D Flow MRI has potential for enabling noninvasive in vivo measurement of WSS, as it evaluates both blood velocity and patient anatomy. Previous work has successfully analyzed aortic WSS from 4D Flow MRI data through two approaches. In the first approach, trained observers select analysis planes along the aorta and segment each plane to explicitly demarcate the endothelium–lumen boundary. These studies then evaluate WSS by numerically approximating the change in velocity perpendicular to these boundary regions at each time point.^{5–12}

In the second approach, trained observers use semi-automatic segmentation packages and interpolation to generate a 3D mesh of the aorta and subsequently evaluate WSS.^{13–17} While these are viable methods for calculating WSS on a case-by-case basis, multiple authors note that their primary limitation is the need for user-input for manual segmentation of the aorta.^{5–7,13–15} Specifically, manual segmentation can lead to inter-observer variability for the lumen boundary as well as potential inaccuracies due to the spatio-temporal interpolations involved in 3D mesh generation. An additional limitation is the sheer number of segmentations required to demarcate regions of interest (ROI) throughout the vasculature over time; the aorta is elastic and hence its boundaries temporally, necessitating manual segmentation at every time point.¹⁵ We, therefore, sought to develop an approach to calculate WSS that is less dependent on user input for initial visualization. To validate our method, we compared our results with those obtained using a reference method by Potters et al.⁸

2 | THEORY

2.1 | Derivation of WSS

The viscous stress vector $\vec{\tau}$ is defined by the dot product of the viscous stress tensor $\bar{\tau}$ and the inward unit normal vector \vec{n} , pointing luminally, for a given blood fluid element⁷:

$$\vec{\tau} = \bar{\tau} \cdot \vec{n}. \quad (1)$$

The viscous stress tensor $\bar{\tau}$ is, in turn, defined by its relationships with the strain rate tensor $\dot{\epsilon}$ of the blood fluid element and the fluid's viscosity η :

$$\bar{\tau} = 2\eta\dot{\epsilon}. \quad (2)$$

We assume that in the area of interest, blood behaves as an incompressible Newtonian fluid with viscosity equal to 3.2 mPa*s.¹⁴ Given a three-dimensional Cartesian space defined by the three axes (x_1, x_2, x_3) and a three-dimensional velocity field (\vec{v}) with corresponding components (v_1, v_2, v_3), we obtain the following strain rate tensor:

$$\dot{\epsilon} = \frac{1}{2} \begin{bmatrix} 2\frac{\partial v_1}{\partial x_1} & \frac{\partial v_1}{\partial x_2} + \frac{\partial v_2}{\partial x_1} & \frac{\partial v_1}{\partial x_3} + \frac{\partial v_3}{\partial x_1} \\ \frac{\partial v_1}{\partial x_2} + \frac{\partial v_2}{\partial x_1} & 2\frac{\partial v_2}{\partial x_2} & \frac{\partial v_2}{\partial x_3} + \frac{\partial v_3}{\partial x_2} \\ \frac{\partial v_1}{\partial x_3} + \frac{\partial v_3}{\partial x_1} & \frac{\partial v_2}{\partial x_3} + \frac{\partial v_3}{\partial x_2} & 2\frac{\partial v_3}{\partial x_3} \end{bmatrix}. \quad (3)$$

Because we are only concerned with the shear component of stress, we set the diagonal components to zero, as they represent orthogonal stresses. As an example, we orient our Cartesian coordinate system such that \vec{n} lies on the x_3 axis. We assume a no-slip boundary condition at the vessel wall boundary and negligible velocity in the direction of the normal. A restatement of these constraints is:

$$\frac{\partial v_i}{\partial x_j} = 0, \quad j \neq 3. \quad (4)$$

For luminal fluid elements, imposing Equation 4 may lead to inaccuracies; however, we tolerate these potential errors for two reasons: (1) we isolate and visualize voxels with high values of shear at the vessel wall and (2) we de-emphasize and ignore voxels within the vessel lumen. As a result of these constraints, our strain rate tensor reduces to:

$$\dot{\epsilon} = \frac{1}{2} \begin{bmatrix} 0 & 0 & \frac{\partial v_1}{\partial x_3} \\ 0 & 0 & \frac{\partial v_2}{\partial x_3} \\ \frac{\partial v_1}{\partial x_3} & \frac{\partial v_2}{\partial x_3} & 0 \end{bmatrix}. \quad (5)$$

Therefore, our shear stress vector at the vessel wall is defined as:

$$\vec{\tau} = \eta \vec{n} \cdot \begin{bmatrix} 0 & 0 & \frac{\partial v_1}{\partial x_3} \\ 0 & 0 & \frac{\partial v_2}{\partial x_3} \\ \frac{\partial v_1}{\partial x_3} & \frac{\partial v_2}{\partial x_3} & 0 \end{bmatrix}. \quad (6)$$

Given the previously used example coordinate system defined by the three axes (x_1 , x_2 , x_3) with \vec{n} lying on axis x_3 as shown previously by Potters et al⁸:

$$\vec{n} = (0, 0, 1). \quad (7)$$

We can now solve for $\vec{\tau}$:

$$\vec{\tau} = \eta \left(\frac{\partial v_1}{\partial x_3}, \frac{\partial v_2}{\partial x_3}, 0 \right). \quad (8)$$

We developed the following algorithm to extrapolate this example coordinate system and derivation to all other fluid elements.

2.2 | Derivation of Algorithm

A restatement of Equation 8 in a static Cartesian coordinate system, in which \vec{n} and x_3 do not necessarily align is:

$$\vec{\tau} = \eta [\vec{n} \cdot \nabla (\vec{v} - (\vec{v} \cdot \vec{n}) \cdot \vec{n})]. \quad (9)$$

We note that $\vec{v} - (\vec{v} \cdot \vec{n}) \cdot \vec{n}$ is the component of velocity parallel to the wall. To approximate the value of \vec{n} , we leverage the 4D flow velocity data. We assume that each blood fluid element has a velocity profile which follows the cardiac cycle and has an associated speed appreciably higher than the surrounding solid elements. That is to say, we use fluid speed as a surrogate for contrast. Therefore, we use a 3D central finite-element scheme to approximate the gradient of fluid speed (s) with second-order error:

$$s = \sqrt{v_1^2 + v_2^2 + v_3^2}. \quad (10)$$

$$\vec{n} \approx \frac{\nabla s}{|\nabla s|}. \quad (11)$$

To enhance visualization of vessel boundaries, we solve:

$$I_{Edge} = |\nabla |\vec{v}| | \circ I \quad (12)$$

where I is the phase contrast MRI signal intensity of a given voxel, and I_{Edge} is the value we assign for visualization of anatomical edges. We chose to define I_{Edge} as the Hadamard product (designated by the open circle in Equation 12) of signal intensity and the magnitude of the gradient of speed to de-emphasize regions with large $|\nabla |\vec{v}| |$ but low MRI signal intensity, notably the lungs.

Having calculated the value of \vec{n} in Equation 10, we can solve for the values of $\vec{\tau}$ in Equation 9 by using a 3D forward/backward finite-element scheme to approximate the

gradient of velocity with second-order error. Specifically, we calculate both the forward and backward finite difference approximation of the derivative for each spatial dimension with second order error to emphasize local abrupt changes in velocity and accentuate WSS over luminal shear stress. Based on the direction of \vec{n} , we then set the antiparallel derivative of velocity to 0 for each spatial dimension. As we are chiefly interested in the value of shear stress at the boundary, the forward and backward difference schemes allow us to approximate the change in velocity at the boundary without erroneously using velocity values within the vessel wall, as would occur with a central difference scheme.

To enhance visualization of WSS near the wall, we solve for fluid speed and calculate the degree of alignment (parallelity) between ∇s and \vec{n} and filter out luminal and extraluminal voxels away from the vessel boundary:

$$parallelity = \nabla s \cdot \vec{n} \quad (13)$$

$$if \ parallelity < 0, \ set \ \vec{\tau} = 0. \quad (14)$$

At the vessel wall, we assume that \vec{n} points toward the center of the lumen. We also assume that fluid speed increases away from the wall as a consequence of the no-slip boundary condition; therefore, ∇s and \vec{n} should generally point in the same direction (the value of Equation 13 should be positive at the wall). Should the normal and gradient of speed vectors be anti-parallel, it is likely that the voxel in question is either a luminal element or is a computational artifact (Supporting Information Figure S1, which is available online).

3 | METHODS

With HIPAA-compliance and IRB approval, we retrospectively identified four 4D Flow MRI acquisitions obtained as part of clinical imaging examinations at our institution. Informed consent was waived by the local Institutional Review Board. The 4D Flow MRI was performed with following administration of intravenous gadolinium contrast (gadobenate dimeglumine, 0.1 mmol/kg) using a cardiac-gated, four-point encoded variable-density pseudo-randomly ordered Cartesian sequence, followed by iterative compressed-sensing and parallel imaging reconstruction with respiratory self-navigation previously described.^{18,19} MR acquisition parameters are shown in Table 1. Calculations of shear stress ($\vec{\tau}$) throughout the vector field were performed in MATLAB 2016b as presented previously.²⁰

We further optimized our methods by using the MATLAB parallel computing toolbox. Volumetric visualization was performed using the Arterys Cardio DL 2.3 (Arterys, San Francisco, CA). For evaluation of WSS, we manually drew the ROI at the vessel-lumen interface in Arterys. We use a previously reported value of 3.2 mPa*s for blood

TABLE 1 4D flow image acquisition parameters and acceleration factors for variable density pseudorandom undersampling are listed below, to target a scan time of approximately 12 min

Case ID	Imaging volume	Acquired resolution (mm) RL × AP × IS	Acquired matrix	Slices	Velocity encoding speed (cm/s)	Temporal resolution (ms)	Acceleration (phase × slice)	Scan time (mm:ss)
1	Sagittal	$3.00 \times 2.50 \times 1.88$	192×256 (AP × IS)	60	250	61	1.8×1.8	13:33
2	Coronal	$2.08 \times 2.80 \times 1.79$	192×224 (RL × IS)	80	200	36	3.2×1.8	11:28
3	Coronal	$1.88 \times 2.80 \times 1.41$	192×256 (RL × IS)	80	250	40	3.0×2.0	12:38
4	Sagittal	$3.00 \times 2.38 \times 1.98$	160×192 (AP × IS)	54	250	50	1.8×1.8	11:12

viscosity.¹⁴ For explicit quantification of WSS, we report two metrics, which are computed at each time step. The first metric is average WSS, which we determined by averaging the WSS within the ROI. The second metric is peak WSS, which is the maximum value of WSS detected within the ROI. The average WSS during peak systole is the maximum value of average WSS with respect to time.

We developed a method for calculation and visualization of WSS, building on previous volumetric techniques (Figure 1).²¹ Specifically, our method first assumes every voxel is at the endothelium-lumen interface and calculates an associated normal vector from velocity data. We then calculate the change in velocity along this normal vector to solve for WSS (Equation 6). Lastly, we visualize all WSS values overlaid onto anatomical data, while preferentially suppressing intraluminal voxels (Equations 13 and 14). The observer is then able to determine locally abnormal regions of WSS at-a-glance and conduct measurements as necessary. We did not perform explicit segmentation in any of the cases presented before quantification. In this manner, our method: (1) uses a

user-independent algorithm for calculating WSS, (2) effectively calculates WSS at every voxel across space and time, and (3) enables rapid localization of regions of aberrant WSS. Finally, our method also leverages parallel computing methods to greatly reduce processing times and enable the automated calculation of WSS through a streamlined computational pipeline. The automated pipeline took approximately 30 min for each case to process every voxel at all time points on a 40 thread CPU system (2x Intel Xeon E5-2670v2) equipped with 132 GB RAM. Our code is available for download on GitHub at <https://github.com/evmasuta/SegFreeWSS>.

To validate our method, we calculated WSS using a reference method.⁸ Specifically, we identified a planar cross-section in the vessel of interest, and created a ROI in this cross section. From this, we calculated WSS analytically from cubic-spline interpolation of the velocity field. We then compared the results from this reference method against our new approach using a two-tailed paired Student's t-test and calculated Pearson's correlation coefficient.

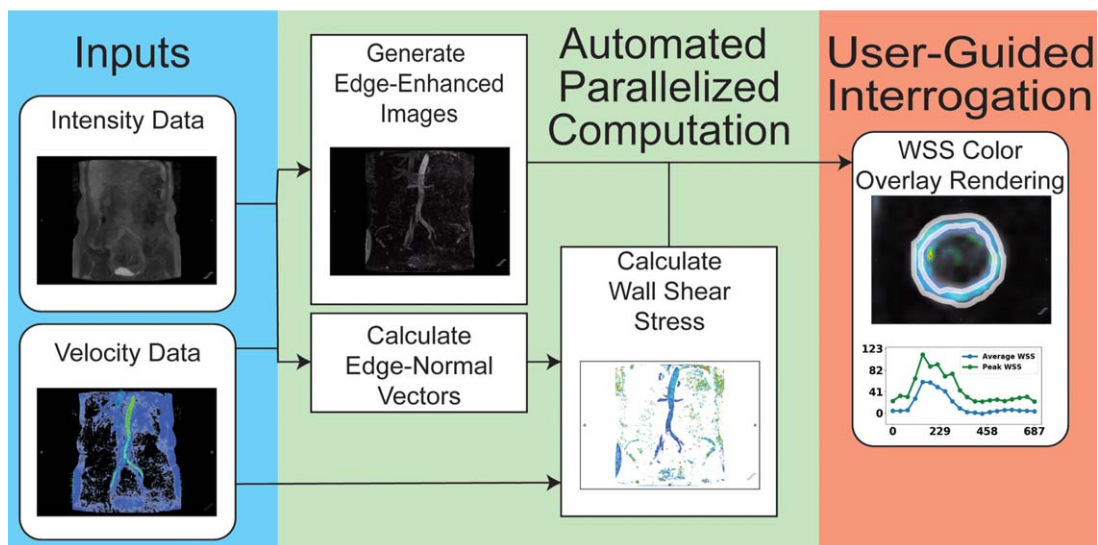


FIGURE 1 Algorithm for determining and visualizing WSS. Input data comprises anatomic and velocity field data from 4D Flow MRI. Fully automated computation calculates edge-enhanced images, edge-normal wall vectors, and WSS from the appropriate input data. In the final step, quantification of specific regions of interest are achieved with user-guided interrogation of the computed WSS fields

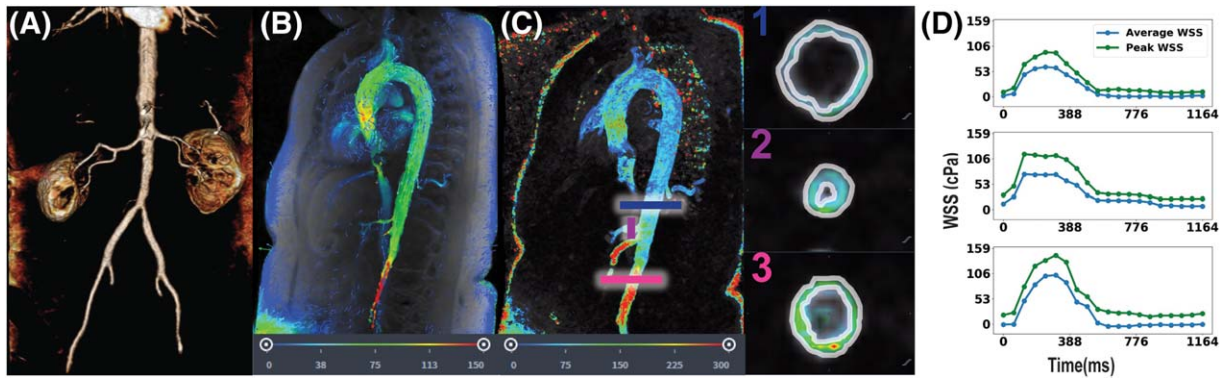


FIGURE 2 MRA (A); 4D Flow MRI visualization, units of cm/s (B); WSS visualization, units of cPa, individual ROIs are color-coded and enumerated (C); WSS quantification for each ROI (white contours) (D). The following three sections were quantified explicitly in (C): (1) distal descending thoracic aorta, (2) celiac artery, (3) infrarenal abdominal aorta. This patient exhibits presumed giant-cell arteritis with locally increased WSS at the site of stenosis in the infrarenal abdominal aorta. Average WSS during peak systole in the normal proximal descending aorta is 62 cPa

4 | RESULTS

We evaluate our algorithm in four subjects previously referred for 4D Flow MRI to illustrate our approach. At-a-glance, it is possible to immediately see general trends of WSS throughout the aorta at every cardiac phase. Furthermore, regions of locally differing WSS are readily visible; regions of stenosis are highlighted (high WSS), whereas regions of aneurysm are de-emphasized (low WSS). Upon localizing any lesions of interest, ROIs can be drawn to quantify WSS over time. Our algorithm allows us to visualize shear stress emphasized near the wall and an experienced user can readily measure WSS at the wall itself and discriminate from artifacts.

In these four cases, we highlight anatomic detail afforded by MRA alongside 4D Flow velocity data and WSS computations. The MRA data delineates anatomic structures in finer detail. Because WSS is derived from velocity data, the 4D Flow velocity field provides a qualitative estimate for the expected WSS behavior. The following cases demonstrate agreement between our complementary datasets; we observe

locally aberrant WSS in regions of gross pathology and abnormal fluid flow as evaluated by MRA and 4D Flow MRI.

Case #1 depicts hemodynamics in a patient with presumed giant cell arteritis involving the infrarenal abdominal aorta as visualized by MRA (Figure 2A). The 4D Flow MRI shows locally increased fluid velocity at the infrarenal abdominal aorta (Figure 2B). We observe elevated average WSS during peak systole (103 cPa) at the site of pathological stenosis relative average WSS during peak systole in the normal distal descending thoracic aorta (62 cPa) (Figures 2C and 2D). Additionally, increased WSS is present at the celiac and superior mesenteric arteries; the average WSS during peak systole in the celiac artery is 74 cPa (Figure 2D).

Case #2 depicts a focal right common iliac artery aneurysm as visualized by MRA (Figure 3A). The 4D Flow MRI shows reduced fluid velocity in an aneurysmal right common iliac artery (Figure 3B). The normal contralateral left common iliac artery provides an internal control for WSS. This case shows the sharp disparity between average WSS during peak systole in the normal (left) common iliac artery (33

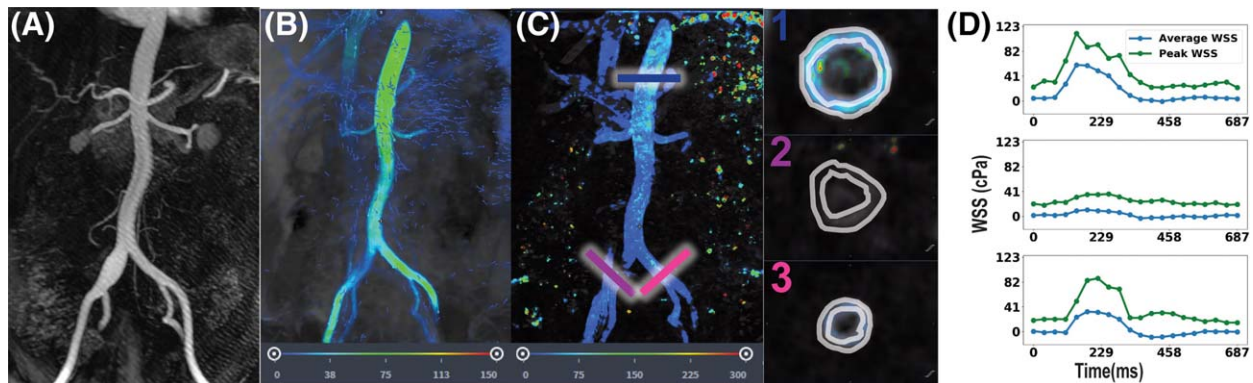


FIGURE 3 MRA (A); 4D Flow MRI visualization, units of cm/s (B); WSS visualization, units of cPa, individual ROIs are color-coded and enumerated (C); WSS quantification for each ROI (white contours) (D). The following three sections were quantified explicitly in (C): (1) distal descending thoracic aorta, (2) aneurysmal right common iliac artery, (3) normal left common iliac artery. There is locally decreased WSS within the right common iliac aneurysm, compared with the normal left common iliac artery. Average WSS during peak systole in the normal proximal descending aorta is 60 cPa

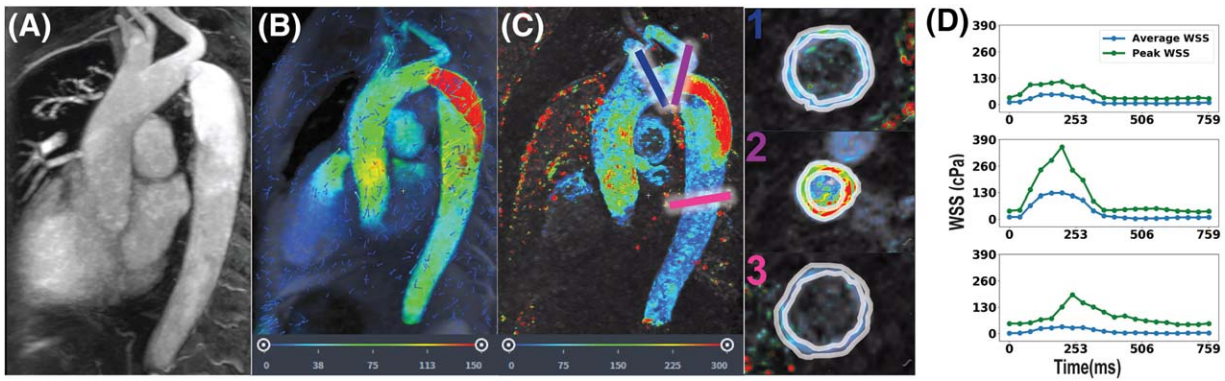


FIGURE 4 MRA (A); 4D Flow MRI visualization, units of cm/s (B); WSS visualization, units of cPa, individual ROIs are color-coded and enumerated (C); WSS quantification for each ROI (white contours) (D). The following three sections were quantified explicitly in (C): (1) aortic arch, (2) site of coarctation, (3) midsagittal thoracic aorta. This patient exhibits aortic coarctation with severe stenosis with locally increased WSS at the site of stenosis and decreased WSS distal to coarctation. Average WSS during peak systole in the normal ascending aorta is 49 cPa

cPa) relative to the average WSS during peak systole in the aneurysmal (right) common iliac artery (10 cPa) (Figures 3C and 3D). Average WSS during peak systole at the distal descending thoracic aorta is consistent with case #1, at 60 cPa (Figure 3D).

Case #3 presents a patient with aortic coarctation with severe stenosis in the distal arch as visualized by MRA (Figure 4A). 4D Flow MRI shows increase fluid velocity at and immediately distal to the site of coarctation (Figure 4B). This case demonstrates focally elevated average WSS during peak systole at the site of stenosis (128 cPa) followed distally by a decrease in average WSS during peak systole to 30 cPa (Figures 4C and 4D). The calculated average WSS during peak systole in the normal ascending aorta proximal to the coarctation is consistent with the previous cases, at 49 cPa (Figure 4D).

Finally, case #4 shows a patient with an aortic dissection as visualized by MRA (Figure 5A). The 4D Flow MRI shows very high fluid velocity within the nearly collapsed aortic true lumen and slow flow within the larger false lumen (Figure 5B). Average WSS during peak systole is high along the course of the intimal flap both proximally (121 cPa) and distally (107 cPa) (Figures 5C and 5D). Proximal to the site

of dissection in the normal segments of the ascending aorta, average WSS during peak systole is 65 cPa, similar to previous subjects (Figure 5D). The slow fluid flow through the false lumen generates negligible WSS.

In normal aortic segments, WSS measurements appear internally consistent in this pilot population of four subjects with this approach. Average WSS during peak systole in normal aorta segments ranged from 49 to 65 cPa, which are similar to previously reported values obtained with other approaches.^{8,10,14,16,22}

When compared against a reference method, we found that our results were moderately correlated (Pearson's $r = 0.52$, $p = 4.4e-36$) and were not statistically different (paired t-test $P = 0.23$, 510 pairs of observations).

5 | DISCUSSION

In this work, we derive a computationally efficient method to approximate WSS, which enables comprehensive visualization of WSS in the large vessels without need for manual contouring. Manual interaction is later leveraged to quantify

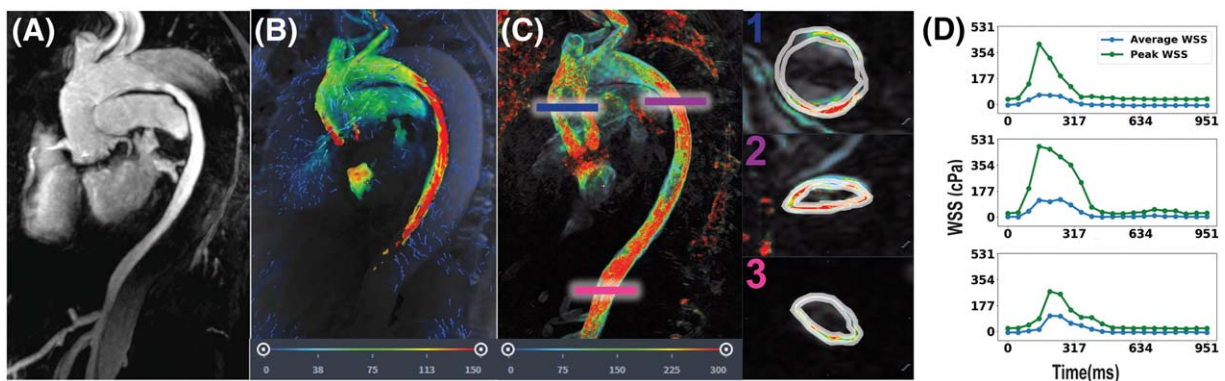


FIGURE 5 MRA (A); 4D Flow MRI visualization, units of cm/s (B); WSS visualization, units of cPa, individual ROIs are color-coded and enumerated (C); WSS quantification for each ROI (white contours) (D). The following three sections were quantified explicitly in (C): (1) ascending aorta, (2) proximal descending thoracic aorta, (3) distal descending thoracic aorta within the aortic dissection. This patient exhibits aortic dissection with locally increased WSS at the site of dissection. Average WSS during peak systole in the normal ascending aorta is 65 cPa

WSS specifically at regions of interest, but is not required for initial visual display of WSS throughout the scanned region. This may bring greater accessibility of WSS visualization into routine clinical practice, and allow clinicians to rapidly focus analysis on regions of grossly abnormal WSS. We opted to construct our algorithm to avoid explicit hyperparameters, which enables this automated visualization.

Regions of high and low WSS may contribute to the formation and evolution of aortic dissection and aneurysm. It has been hypothesized that locally high WSS may activate WSS-dependent vasodilatory and remodeling mechanisms.¹ The case of aortic coarctation presented here is suggestive that certain sections of the aortic wall may experience a greater tendency toward remodeling than others. It is worth noting that our estimates for average WSS during peak systole in nonpathological regions of the aorta are similar to “normal” values reported in the literature (approx. 60 cPa).^{8,10,14,16,22} Our method offers two main potential advantages. The first advantage, the user-independent implicit display of WSS eliminates potential mismatch between the fluid velocity boundary and user-defined boundaries for calculation of WSS.

The second advantage of our method is that, for qualitative evaluation of WSS, calculations are fully automated. Traditional methods for calculating WSS heavily rely on presegmentation of the vasculature; ideally, the classification of edge vs. lumen should be performed for every voxel at every time point for accurate quantification of WSS. Current methods either solely rely on manual segmentation, which comes with implicit user biases and inaccuracies, or with semi-automated methods which expedite the process by averaging frames and/or using splines.^{5–17} While efficient, use of splines is sensitive to a variety of hyperparameters such as the specific position of the nodes.⁸

Our proposed algorithm relies solely on empirical data to classify voxels as edge or lumen and is, therefore, both user-independent and inherently reproducible. It is now possible to automatically evaluate large patient cohorts in parallel. From a clinical perspective, rapid processing of patient 4D Flow MRI data may streamline screening and diagnostics. From a research perspective, the ability to rapidly process large datasets in a reproducible manner permits the generation and evaluation of novel hypotheses correlating pathological WSS with disease states.

In addition to calculating systolic WSS where WSS is the highest, our method may be generalizable to other portions of the cardiac cycle (Supporting Information Video S1). However, during phases of the cardiac cycle with lower velocity, such as diastolic phases, or in vessels with complex geometry, the gradient of speed may become less reliable as an estimate of the wall normal. In situations where the vessel wall does not move or angulate considerably during the cardiac cycle, it is possible extrapolate the systolic wall normal to other cardiac phases. Evaluation and refinement of this approach is a potential subject of future investigation.

The visualization strategy we present here may depend on the quality of the underlying image data. We perform 4D Flow MRI at our institution using a postcontrast technique with compressed-sensing and modest acceleration factors to maximize image quality. It is possible that the visualization strategy presented here may not work as well with low signal-to-noise image data or in examinations performed without contrast. In addition, it is possible that, with blood pool contrast agents such as ferumoxytol, the quality of WSS calculations may further improve due to improvements in SNR. In our brief study, we did not fully examine these potential contributing factors, but they can be undertaken in future work.

Additionally, our study is limited by the small number of cases analyzed. For this pilot study, we were primarily interested in demonstrating a proof-of-concept and the subject of future work will be to assess large patient and control cohorts to begin construction of classifiers to differentiate between normal and pathological states. From a theoretical perspective, our method is limited by the current spatiotemporal resolution. Because the greatest change in fluid velocity occurs immediately proximal to the vessel wall, poor resolution can lead to error in the WSS approximation. It is the authors' belief that, as measurement methods gain resolution, the results generated by our algorithm will reflect more accurately the true value of WSS.

6 | CONCLUSIONS

We present a novel method to calculate and visualize WSS from 4D Flow MRI data, using implicit rather than user-defined boundaries. Our method leverages parallel processing and removes the upfront need for segmentation, which may enable greater accessibility for more routine clinical use. Furthermore, our method performs comparably to a previously published reference algorithm. Our method allows for at-a-glance localization of aberrant WSS and subsequent targeted quantification. These advantages may enable greater accessibility of WSS for potential use in a clinical setting by streamlining the computational and analytical processes. Future work may include further refinement of the algorithm to account for vessel contractility (i.e. evaluating the hemodynamic effects of the radial component of fluid velocity), assessment of its sensitivity to acquired spatial resolution, and application of the technique to study WSS in specific patient populations.

ACKNOWLEDGMENTS

We thank the members of the Hsiao lab and Dr. Neil Chi for advice regarding this manuscript. We also thank Travis T. Tanaka and Dr. Gerard Nihous for proofreading the theory of our work and providing helpful insights.

CONFLICT OF INTEREST

Dr. Albert Hsiao is a founder, consultant, and shareholder of Arterys, Inc.

ORCID

Francisco Contijoch  <http://orcid.org/0000-0001-9616-3274>

Joseph Cheng  <http://orcid.org/0000-0002-6559-0473>

Albert Hsiao  <https://orcid.org/0000-0002-9412-1369>

REFERENCES

- [1] Cunningham KS, Gotlieb AI. The role of shear stress in the pathogenesis of atherosclerosis. *Lab Invest.* 2005;85:9-23.
- [2] Bäck M, Gasser TC, Michel JB, Caligiuri G. Biomechanical factors in the biology of aortic wall and aortic valve diseases. *Cardiovasc Res.* 2013;99:232-241.
- [3] Macura KJ, Corl FM, Fishman EK, Bluemke DA. Pathogenesis in acute aortic syndromes: aortic dissection, intramural hematoma, and penetrating atherosclerotic aortic ulcer. *AJR Am J Roentgenol.* 2003;181:309-316.
- [4] Cecchi E, Giglioli C, Valente S, et al. Role of hemodynamic shear stress in cardiovascular disease. *Atherosclerosis.* 2011;214:249-256.
- [5] Harloff A, Nussbaumer A, Bauer S, et al. In vivo assessment of wall shear stress in the atherosclerotic aorta using flow-sensitive 4D MRI. *Magn Reson Med.* 2010;63:1529-1536.
- [6] Markl M, Wallis W, Harloff A. Reproducibility of flow and wall shear stress analysis using flow-sensitive four-dimensional MRI. *J Magn Reson Imaging.* 2011;33:988-994.
- [7] Stalder AF, Russe MF, Frydrychowicz A, Bock J, Hennig J, Markl M. Quantitative 2D and 3D phase contrast MRI: optimized analysis of blood flow and vessel wall parameters. *Magn Reson Med.* 2008;60:1218-1231.
- [8] Potters WV, van Ooij P, Marquering H, van Bavel E, Nederveen AJ. Volumetric arterial wall shear stress calculation based on cine phase contrast MRI. *J Magn Reson Imaging.* 2015;41:505-516.
- [9] Frydrychowicz A, Stalder AF, Russe MF, et al. Three-dimensional analysis of segmental wall shear stress in the aorta by flow-sensitive four-dimensional MRI. *J Magn Reson Imaging.* 2009;30:77-84.
- [10] Burk J, Blanke P, Stankovic Z, et al. Evaluation of 3D blood flow patterns and wall shear stress in the normal and dilated thoracic aorta using flow-sensitive 4D CMR. *J Cardiovasc Magn Reson.* 2012;14:84.
- [11] Oyre S, Ringgaard S, Kozerke S, et al. Accurate noninvasive quantitation of blood flow, cross-sectional lumen vessel area and wall shear stress by three-dimensional paraboloid modeling of magnetic resonance imaging velocity data. *J Am Coll Cardiol.* 1998;32:128-134.
- [12] Efstathopoulos EP, Patatoukas G, Pantos I, Benekos O, Katritsis D, Kelekis NL. Wall shear stress calculation in ascending aorta using phase contrast magnetic resonance imaging. Investigating effective ways to calculate it in clinical practice. *Phys Med.* 2008;24:175-181.
- [13] van Ooij P, Potters WV, Collins J, et al. Characterization of abnormal wall shear stress using 4D flow MRI in human bicuspid aortopathy. *Ann Biomed Eng.* 2015;43:1385-1397.
- [14] van Ooij P, Powell AL, Potters WV, Carr JC, Markl M, Barker AJ. Reproducibility and interobserver variability of systolic blood flow velocity and 3D wall shear stress derived from 4D flow MRI in the healthy aorta. *J Magn Reson Imaging.* 2016;43:236-248.
- [15] Piatti F, Sturla F, Bissell MM, et al. 4D Flow analysis of BAV-related fluid-dynamic alterations: evidences of wall shear stress alterations in absence of clinically-relevant aortic anatomical remodeling. *Front Physiol.* 2017;8:441.
- [16] Biegling ET, Frydrychowicz A, Wentland A, et al. In vivo 3-dimensional magnetic resonance wall shear stress estimation in ascending aortic dilation. *J Magn Reson Imaging.* 2011;33:589-597.
- [17] Renner J, Najafabadi HN, Modin D, Lanne T, Karlsson M. Subject-specific aortic wall shear stress estimations using semi-automatic segmentation. *Clin Physiol Funct Imaging.* 2012;32:481-491.
- [18] Vasanawala SS, Hanneman K, Alley MT, Hsiao A. Congenital heart disease assessment with 4D flow MRI. *J Magn Reson Imaging.* 2015;42:870-886.
- [19] Cheng JY, Hanneman K, Zhang T, et al. Comprehensive motion-compensated highly accelerated 4D flow MRI with ferumoxylol enhancement for pediatric congenital heart disease. *J Magn Reson Imaging.* 2016;43:1355-1368.
- [20] Masutani EM, Cheng JY, Alley MT, Vasanawala SS, Hsiao A. Volumetric segmentation-free method for quantitative visualization of cardiovascular wall shear stress using 4D flow MRI. In Proceedings of the 25th Annual Meeting of ISMRM, Honolulu, HI, 2017. Abstract 2846.
- [21] Hsiao A, Lustig M, Alley MT, Murphy MJ, Vasanawala SS. Evaluation of valvular insufficiency and shunts with parallel-imaging compressed-sensing 4D phase-contrast MR imaging with stereoscopic 3D velocity-fusion volume-rendered visualization. *Radiology.* 2012;265:87-95.
- [22] Sugimoto K, Shimamura Y, Tezuka C, et al. Effects of arterial blood flow on walls of the abdominal aorta: distributions of wall shear stress and oscillatory shear index determined by phase-contrast magnetic resonance imaging. *Heart Vessels.* 2016;31:1168-1175.

SUPPORTING INFORMATION

Additional Supporting Information may be found in the online version of this article.

FIGURE S1 A, WSS visualization of case #4 (aortic dissection) with normal vector field overlaid (white arrows) before filtering out luminal shear voxels, B, application of Theory equations 13 and 14 to filter out luminal shear elements to optimize visualization of shear stress near the wall

VIDEO S1 WSS visualization of case #1 (presumed giant cell arteritis) across all phases of the cardiac cycle. Scale is the same as in Figure 2C

How to cite this article: Masutani EM, Contijoch F, Kyubwa E, et al. Volumetric segmentation-free method for rapid visualization of vascular wall shear stress using 4D flow MRI. *Magn Reson Med.* 2018;00:1–8. <https://doi.org/10.1002/mrm.27159>